

Chapter 5

Reflector Modelling

It was shown that the existing Gaussian model used to represent the transverse plane reflector pattern in Section 2.5 was inaccurate for scan angles outside the $\pm 30^\circ$ range. These inaccuracies occur because the simplified model does not consider the electromagnetic scattering between the reflector and ground plane, and reflector curvature. This Chapter presents a new transverse plane reflector model, which will include these refinements. This model enables the calculation of the half-power feed beamwidth (HPBW) range for optimum sensitivity, which is required for the line feed development in Chapter 6. The model is also used in a focal region analysis, to evaluate the performance of the two feed configurations described in Section 4.3.

This chapter begins with a section describing the approach used for the proposed reflector model. Section 5.2 analyses the separation of the electromagnetic field into transverse magnetic (TM) and transverse electric components (TE). An overview of the underlying theory is described in Sections 5.3.1 and 5.3.2. The program used for solving the electromagnetic fields for the cylindrical reflector is described in Section 5.4. Feed patterns with varying half-power beamwidths are presented in Section 5.5 and selecting the feed beamwidth range for optimum aperture efficiency and spillover temperature is described in Section 5.5.1. Section 5.6 investigates the reflector pattern performance with a combined feed and reflector analysis. Section 5.6.1 describes the reflector pattern performance for changes in the feed position, to investigate the reflector phase centre and defocusing conditions. Section 5.6.2 presents an assessment of the selected feed beamwidth range. A beamwidth matching analysis presented in Section 5.6.3 describes a method of minimising edge effects from the finite ground plane for the TE component. Section 5.6.4 describes the performance of the reflector pattern over a 2:1 bandwidth to investigate the gain variation with frequency caused by the standing wave between the reflector vertex and feed ground plane.

5.1 Modelling Technique

Limitations in the current transverse plane beam model (a Gaussian representation) resulted in a new model described in Section 2.5.1. The Gaussian model does not consider the reflector curvature, line feed ground plane blockage or feed pattern variation with scanning angle. In addition, parameters such as aperture efficiency, noise temperature and sidelobe levels across the scan angle range are not readily incorporated. The proposed model involves analysing the reflector radiation performance for a prescribed line feed radiation pattern. This assumes that the line feed and the reflector can be analysed separately, which is justified because the line feed is in the far-field of

the reflector and mutual coupling between them is negligible. However, mutual coupling does occur between elements in the line feed, as described in Section 6.1.1.

The approach in this chapter considers the reflector and line feed ground plane geometries. A feed model is used to produce transverse line feed patterns, which are analysed to determine parameters such as spillover temperature and taper efficiency. The feed model is then included in a combined feed and reflector model, which generates a set of currents on the reflector. These surface currents are then integrated and added to the currents generated from the feed model to produce the reflector pattern. From this pattern, parameters such as reflector antenna temperature, half-power beamwidth and sidelobe levels can be obtained. Common methods to determine radiation patterns for reflector antennas include optical or full-wave methods. Both methods involve the application of Maxwell's equations and the use of boundary conditions to solve for the surface currents.

Optical methods, such as physical optics (PO) can be used in calculating the reflector currents when its size is much larger than the operating wavelength. The method assumes that the feed produces a plane wave at the reflector and that the reflector behaves as a perfect electrical conducting (PEC) surface. The surface current on the reflector is given by:

$$\mathbf{J}_s = \hat{\mathbf{n}} \times \mathbf{H} \quad (5.1)$$

Where $\hat{\mathbf{n}}$ = unit normal vector to the conducting surface

\mathbf{H} = total magnetic field

Because the reflector is a perfect conductor, the incident field \mathbf{H}_i is equal to the reflected field \mathbf{H}_r ; therefore the surface current becomes:

$$\mathbf{J}_s = \begin{cases} 2\hat{\mathbf{n}} \times \mathbf{H}_i & \text{on the front of the reflector} \\ 0 & \text{on the shadow side of the reflector} \end{cases} \quad (5.2)$$

The PO method neglects the contribution from currents in the 'shadow' region to the main beam and sidelobes. Diffraction effects at the edges of the reflector, and ground plane blockage and standing waves due to the feed are also neglected. An advantage of the PO method is faster computation for reflectors with electrically large geometries when compared to a full-wave method, because the surface currents on the front of the reflector are found directly without the need for matrix inversion. Although this method is accurate in determining the reflector pattern for the main beam and the first few sidelobes, accuracy outside this region is degraded by reflector edge diffraction effects (Stutzman and Thiele 1998). Additional diffraction terms to model these effects increase the complexity of the solution.

A full-wave method, such as method of moments (MoM), divides the reflector into cells and solves for the surface current on each cell. The formulation requires an excitation vector $[V]$, to represent the incident field from the feed, and an impedance matrix $[Z]$, to represent the coupling between the reflector cells, as in Equation 5.3. The unknown surface currents are contained in the vector $[J_s]$.

$$[Z][J_s] = [V_i] \quad (5.3)$$

Equation 5.3 is then solved by matrix inversion techniques to obtain the surface current vector, corresponding to points on the reflector cells. An advantage of this method is that the solution is rigorous when compared to optical methods. Surface currents are determined in all regions of the scatterer by applying the appropriate boundary conditions. Diffraction terms are unnecessary, as scattering from the reflector edge and line feed ground plane are incorporated into the impedance matrix. The accuracy of the method can be improved by reducing the reflector cell size. However, computation time increases with the electrical size. Other full-wave methods such as the finite difference time domain and finite element method have been applied successfully to reflector analysis (Luo et al. 2002).

For the reflector analysis, a full-wave method of moments approach is used to calculate the surface currents. Because the analysis occurs in the transverse plane, a two-dimensional geometry is considered, producing manageable computation time. A rigorous approach can also confirm whether an optical method has sufficient accuracy to model the MOST reflector geometry at frequencies where the full-wave method becomes computationally intensive. Formulation of the electromagnetic theory applied to a cylindrical reflector geometry and the corresponding method of moments solution is described in Section 5.3. Although the MOST reflector is constructed using a wire mesh, it is considered a PEC for modelling purposes. The planned mesh spacing for SKAMP is 6×6 mm, which is a fraction of a wavelength at the highest operating frequency, producing a reflector with minimal leakage. The MOST reflector geometry in the transverse plane uses purlins to approximate the curvature of a parabola in a piecewise configuration. This approximation is accurate for frequencies up to 2 GHz where pattern degradation becomes significant (Vinogradov et al. 2005).

5.2 Polarisation Definitions

A cylindrical reflector can be modelled as a rectangular aperture (Section 2.2). Because the geometry can be assumed invariant in the longitudinal dimension, the modelling can be simplified from a three-dimensional problem to a two-dimensional one. In two dimensions, the electromagnetic (EM) fields can be separated into transverse magnetic (TM) and transverse electric (TE) field components with respect to the longitudinal dimension. These components are excited by either a z -directed current, J_z , or a transverse current, J_t , as shown in Figure 5.1, along with the coordinate system used for reflector modelling. The TM and TE components can then be combined to produce the desired polarisation state.

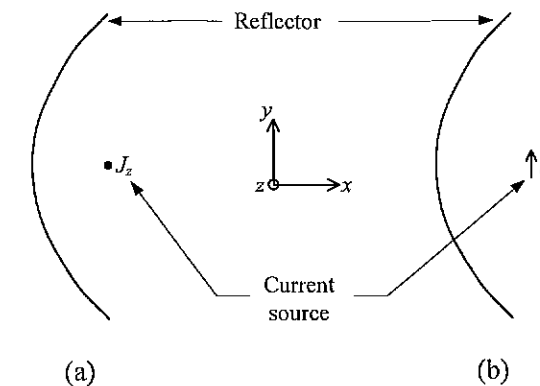


Figure 5.1 Reflector geometry in the transverse plane with a current source shown at the focal point. (a) Transverse magnetic component. (b) Transverse electric component.

The feed polarisation orientation selected for the line feed was dual linear polarisation, as described in Section 3.3.4. The convention used to describe the polarisation is defined as horizontal or vertical with respect to the z -direction, as depicted in Figure 5.2.

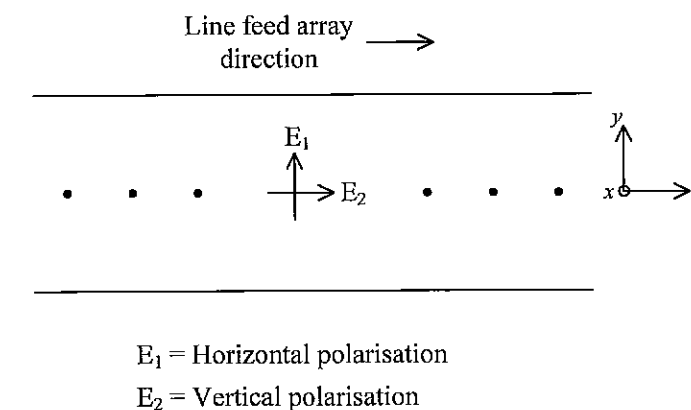


Figure 5.2 Line feed geometry, showing the orientation of the dual linear polarisation configuration.

Furthermore each polarisation has co- and cross-polar components, which correspond to either a TM or TE component. The relationship between the polarisations and the corresponding field component are given in Table 5.1.

Polarisation	Co-polar	Cross-polar
Vertical	TM	TE
Horizontal	TE	TM

Table 5.1 Relationship between co- and cross-polar components and TM and TE components for a dual linear polarisation configuration.

5.3 Electromagnetic Theory

The theory to derive the transverse magnetic and electric fields is described, following Harrington (1961) and Peterson et al. (1998).

Currents induced on the reflector by the line feed can be determined by solving Maxwell's equations with induced polarisation currents and charges, given in Equation 5.4, in time-harmonic form and suppressing the $e^{j\omega t}$ factor.

$$\nabla \times \mathbf{E} = -j\omega\mu\mathbf{H} - \mathbf{M} \quad (5.4a)$$

$$\nabla \times \mathbf{H} = j\omega\epsilon\mathbf{E} + \mathbf{J} \quad (5.4b)$$

$$\nabla \cdot \epsilon\mathbf{E} = \rho_e \quad (5.4c)$$

$$\nabla \cdot \mu\mathbf{H} = \rho_m \quad (5.4d)$$

$$\nabla \cdot \mathbf{J} = -j\omega\rho_e \quad (5.4e)$$

Where \mathbf{E} is the electric field intensity, \mathbf{H} is the magnetic field intensity, \mathbf{M} is the magnetic current, \mathbf{J} is the electric current, ω is the angular frequency, μ is the permeability, ϵ is the permittivity, ρ_e is the electric charge and ρ_m is the magnetic charge.

Although magnetic currents and charges are fictitious, they are useful as equivalent sources for complicated electric fields (Stutzman and Thiele 1998).

Maxwell's Equations applied at the boundary of two homogeneous regions, 1 and 2, is depicted in Figure 5.3 and a set of boundary conditions in time harmonic form can be expressed as:

$$\hat{\mathbf{n}} \times (\mathbf{H}_1 - \mathbf{H}_2) = \mathbf{J}_s \quad (5.5a)$$

$$(\mathbf{E}_1 - \mathbf{E}_2) \times \hat{\mathbf{n}} = \mathbf{M}_s \quad (5.5b)$$

Where the electric, \mathbf{J}_s , and magnetic, \mathbf{M}_s , surface currents are flowing at the boundary between the two homogenous regions and the unit vector normal, $\hat{\mathbf{n}}$, to the boundary is directed from region 2 into 1.

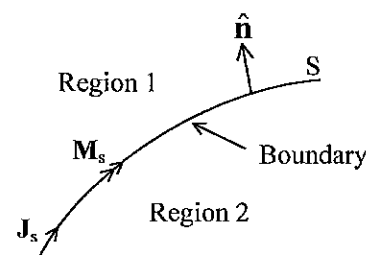


Figure 5.3 Electric and magnetic currents flowing on the surface, S , between two homogenous regions.

For a perfect conducting surface on one side of the homogeneous region in Figure 5.3, the tangential electric field vanishes and the boundary conditions become:

$$\hat{\mathbf{n}} \times \mathbf{H} = \mathbf{J}_s \quad (5.6a)$$

$$\hat{\mathbf{n}} \times \mathbf{E} = 0 \quad (5.6b)$$

The electric (\mathbf{E}) and magnetic (\mathbf{H}) field intensities can be represented by scalar and vector potentials to decouple the curl equations and allow an easier construction of TM and TE solutions for the surface currents. For a known current source such as a line feed, \mathbf{J} , the electric scalar, Φ_e , and magnetic vector potential, \mathbf{A} , functions can be introduced to simplify the solution for the \mathbf{E} and \mathbf{H} fields from Equation 5.4(a) and 5.4(b). A similar solution is obtained using the magnetic scalar and electric vector potential functions Φ_h and \mathbf{F} by duality (Harrington 1961).

Due to the divergenceless character of Equation 5.4(d), $\rho_m = 0$, it can be represented as the curl of some vector function:

$$\mathbf{H} = \nabla \times \mathbf{A} \quad (5.7)$$

The curl of \mathbf{A} is defined but its divergence has not been specified. Substituting Equation 5.7 into 5.4(a), and assuming no magnetic currents, gives:

$$\nabla \times (\mathbf{E} + j\omega\mu\mathbf{A}) = 0 \quad (5.8)$$

Since the curl of the electric field, $\mathbf{E} + j\omega\mu\mathbf{A}$, is equal to zero, it is a conservative field and behaves like a static electric field. Therefore, an electric scalar potential can be defined as Φ_e and Equation 5.8 becomes:

$$\mathbf{E} = -j\omega\mu\mathbf{A} - \nabla\Phi_e \quad (5.9)$$

Both \mathbf{E} and \mathbf{H} fields are now expressed in terms of potential functions, which can be solved in order to obtain the fields.

Substituting Equation 5.7 into 5.4(b) gives:

$$\nabla \times \nabla \times \mathbf{A} = j\omega\epsilon\mathbf{E} + \mathbf{J} \quad (5.10)$$

Using the identity: $\nabla \times \nabla \times \mathbf{A} = \nabla(\nabla \cdot \mathbf{A}) - \nabla^2 \mathbf{A}$, Equation 5.10 becomes:

$$(\nabla(\nabla \cdot \mathbf{A}) - \nabla^2 \mathbf{A}) = j\omega\epsilon\mathbf{E} + \mathbf{J} \quad (5.11)$$

Substituting Equation 5.9 into 5.11 gives:

$$\nabla^2 \mathbf{A} + \omega^2 \epsilon \mu \mathbf{A} - \nabla(\Phi_e + \nabla \cdot \mathbf{A}) = -\mathbf{J} \quad (5.12)$$

The divergence of \mathbf{A} is yet to be specified and it can be selected so the third term of Equation 5.12 is cancelled if

$$\nabla \cdot \mathbf{A} = -\Phi_e \quad (5.13)$$

This is known as the Lorentz condition. Using this condition, Equation 5.12 becomes:

$$\nabla^2 \mathbf{A} + \omega^2 \epsilon \mu \mathbf{A} = -\mathbf{J} \quad (5.14)$$

Equation 5.14 is the vector wave equation and can be solved for \mathbf{A} in a cylindrical coordinate system to determine the reflector surface currents. \mathbf{A} can be substituted into Equation 5.7 to determine the magnetic field \mathbf{H} ; the electric field \mathbf{E} can be obtained by substituting \mathbf{H} into Equation 5.4(a). The solution of the wave equation using scalar and vector potentials to obtain TM and TE components of the electromagnetic fields are presented next.

5.3.1 Transverse Magnetic (TM) Formulation

In a transverse magnetic formulation, consider a z -directed line current, I , in the cylindrical coordinate system shown in Figure 5.4.

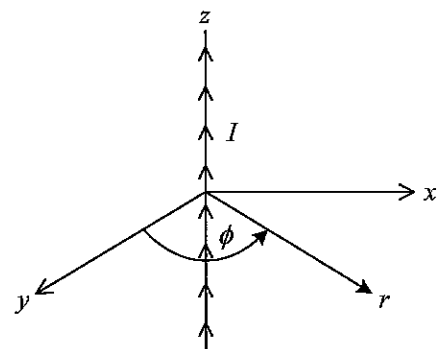


Figure 5.4 Cylindrical coordinate system showing a z -directed line current source.

The scalar wave equation describes the radiation from the line current:

$$\nabla^2 \psi + \omega^2 \mu \epsilon \psi = 0 \quad (5.15)$$

Where the z -directed magnetic vector potential is represented by $A_z = \psi$. The TM field induced by the current source I at a point r can be solved by finding solutions to the scalar wave equation in cylindrical coordinates. A solution for an outward travelling cylindrical wave is given by (Harrington 1961):

$$A_z = \frac{1}{4j} H_0^{(2)}(kr) \quad (5.16)$$

Where $H_0^{(2)}$ is the Hankel function of the second kind and first order, which represents the propagation behaviour of an outward travelling cylindrical wave.

An electric field integral equation (EFIE) formulation is used to determine the z -directed electric field, E_z , at point r due to a line current, I , by substituting Equation 5.16 into 5.9, assuming there are no scalar potential electric sources in the formulation:

$$E_z = -\frac{k\eta}{4} I H_0^{(2)}(kr) \quad (5.17)$$

Where η is the free-space impedance and k is the wave number of the medium.

Equation 5.17 represents the field E_z at r when the current source is directed along the z -axis. Fields for a current source parallel to the z -axis can be evaluated by specifying the field and source points with vectors:

$$r = \mathbf{u}_x x + \mathbf{u}_y y \quad \text{field point}$$

$$r' = \mathbf{u}_x x' + \mathbf{u}_y y' \quad \text{source point}$$

The distance between the source and field points is shown in Figure 5.5 and given by:

$$\begin{aligned} |r - r'| &= \sqrt{(x - x')^2 + (y - y')^2} \\ &= \sqrt{r^2 + r'^2 - 2rr' \cos(\phi - \phi')} \end{aligned}$$

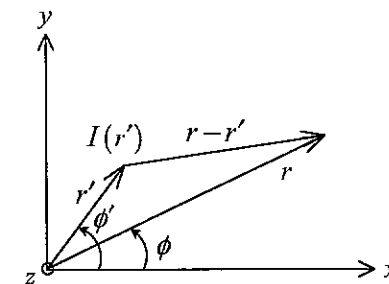


Figure 5.5 Line current source displaced parallel to the z -axis at r' .

The z -directed vector magnetic potential, A_z , and electric field, E_z , at a point r due to a line current at r' are:

$$A_z(r) = \frac{I(r')}{4j} H_0^{(2)}(k|r - r'|) \quad (5.18)$$

$$E_z(r) = -\frac{k\eta}{4} I(r') H_0^{(2)}(k|r - r'|) \quad (5.19)$$

The electric field for a PEC reflector due to a line current, I , can be determined by calculating E_z at points on the reflector and then integrating over a cross section of the source dA :

$$E_z(r) = -\frac{k\eta}{4} \iint I(r') H_0^{(2)}(k|r - r'|) dA \quad (5.20)$$

For the cylindrical reflector, the z -directed line source has an incident electric field E_z^{inc} , which illuminates a reflector and induces a scattered current J_z on the surface. The total electric field is calculated by summing the incident and scattered fields. For a PEC, the boundary condition in Equation 5.6(b) can be enforced at the reflector surface, S , to obtain:

$$E_z^{tot} = E_z^{inc} + E_z^s = 0 \quad (5.21)$$

Hence,

$$E_z^{inc} = -E_z^s \quad (5.22)$$

In the formulation we assume the scattered field, E_z^s , and current J_z are unknown and the incident electric field, E_z^{inc} , is known:

$$E_z^{inc}(r) = -j\omega\mu A_z^{inc} \quad (5.23)$$

The scattered field at r due to E_z can be determined using delta weighting functions at points along the scatterer curvature, S , shown in Figure 5.6 and given by:

$$E_z^s(r) = -\frac{k\eta}{4} \int J_z(r') H_0^{(2)}(k|r-r'|) ds' \quad (5.24)$$

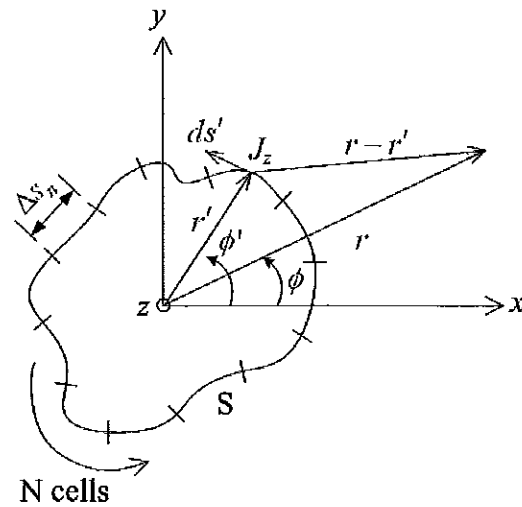


Figure 5.6 Representation of cylindrical scatterer geometry for method of moments formulation.

Substituting Equation 5.24 into 5.22 gives:

$$E_z^{inc}(r) = \frac{k\eta}{4} \int J_z(r') H_0^{(2)}(k|r-r'|) ds' \quad (5.25)$$

To calculate the unknown scattered current, J_z , the reflector can be divided into cells approximating the contour of the reflector shown in Figure 5.6. The equivalent current at each cell is determined by approximating the current distribution using basis functions. Using pulse basis functions, p_n , to represent the current gives:

$$p_n(s) = \begin{cases} 1 & \text{if } s \in \text{cell } n \\ 0 & \text{otherwise} \end{cases} \quad (5.26)$$

So the current J_z can be approximated by:

$$J_z(s) \cong \sum_{n=1}^N a_n p_n(s) \quad (5.27)$$

Substituting J_z into Equation 5.25 gives:

$$E_z^{inc}(s) \cong \frac{k\eta}{4} \sum_{n=1}^N a_n \int_{\Delta s_n} H_0^{(2)}(k|r-r'|) ds' \quad (5.28)$$

This equation involves solving the N unknown coefficients, a_n , at the centre of the cells, from which J_z is determined by Equation 5.27. Impedance matrix elements can be defined by Equation 5.29 by recognising that Equation 5.28 resembles Ohm's law:

$$Z_{mn} = \frac{k\eta}{4} \int_{\Delta s_n} H_0^{(2)}(k|r-r'|) ds' \quad (5.29)$$

with the voltage elements:

$$V_m = E_z^{inc}(s) \quad (5.30)$$

this gives an $N \times N$ system of linear equations:

$$\begin{bmatrix} E_z^{inc}(s_1) \\ E_z^{inc}(s_2) \\ E_z^{inc}(s_3) \\ \vdots \\ E_z^{inc}(s_N) \end{bmatrix} = \begin{bmatrix} Z_{11} & Z_{12} & Z_{13} & \cdots & Z_{1N} \\ Z_{21} & Z_{22} & Z_{23} & \cdots & Z_{2N} \\ Z_{31} & Z_{32} & Z_{33} & \cdots & Z_{3N} \\ \vdots & \vdots & \vdots & \ddots & \vdots \\ Z_{N1} & Z_{N2} & Z_{N3} & \cdots & Z_{NN} \end{bmatrix} \begin{bmatrix} a_1 \\ a_2 \\ a_3 \\ \vdots \\ a_N \end{bmatrix} \quad (5.31)$$

with appropriate accuracy, a numerical integration technique can be employed to determine the mutual impedance elements, Z_{mn} . Alternatively, these elements can be evaluated by assuming each current element, $J_z \Delta s_n$, as a filament of current when the field point is not on Δs_n :

$$Z_{mn} \approx \frac{k\eta}{4} \Delta s_n H_0^{(2)}(k|r-r'|) \quad (5.32)$$

The self-impedance entities, Z_{nn} , are larger than the mutual-impedances, Z_{mn} , and are more significant to the solution in Equation 5.31. However, the Hankel function has an integrable singularity for these elements: i.e. at $H_0^{(2)}(0)$ and are evaluated analytically using the small argument form for the Hankel function (Harrington 1961):

$$Z_{nn} \approx \frac{k\eta}{4} \Delta s_n \left[1 - j \frac{2}{\pi} \log_e \left(\frac{\gamma k \Delta s_n}{4e} \right) \right] \quad (5.33)$$

Where $\gamma = 0.5772$ is Euler's constant and $e = 2.718$.

5.3.2 Transverse Electric (TE) Formulation

In the transverse electric formulation, shown in Figure 5.1(b), the electric field vector of the source is aligned in a direction transverse to the z -directed line feed. The induced reflector surface currents, J_t , flow in a direction tangential to the reflector surface. Due to

the direction of the current, the use of pulse basis functions to approximate the current density has a singularity at the edges of each separate cell. To eliminate this singularity, triangular basis functions are used which force the current to zero at the edges of the cell. Either an electric field (EFIE) or magnetic field (MFIE) integral equation can be used depending on the problem geometry and ease of constructing a solution. An EFIE, in Equation 5.9, is used to construct a TE solution because its boundary conditions enable the modelling of infinitely thin scatterers such as a reflector. The theory presented for the TE formulation follows directly from Peterson et al. (1998).

The EFIE applied for the TE case is given by:

$$\hat{t} \cdot E^{inc} = \hat{t} \cdot (jk\eta A + \nabla \Phi_e) \quad (5.34)$$

Where \hat{t} represents the unit vector directed along the transverse orientation of the reflector strip and E^{inc} is the incident electric field.

The transversely directed magnetic vector potential is given by:

$$A(r) = \frac{1}{4j} \int_{\text{strip}} \hat{t}(r') J_t(r') H_0^{(2)}(k|r-r'|) ds' \quad (5.35)$$

and the electric scalar vector potential is:

$$\Phi_e(r) = \frac{1}{4j\epsilon_0} \int_{\text{strip}} \rho_e(r') H_0^{(2)}(k|r-r'|) ds' \quad (5.36)$$

the electric surface charge density, ρ_e , is related to the current through the equation of continuity:

$$\rho_e(r) = \frac{j}{\omega} \frac{\partial J_t(r)}{\partial s} \quad (5.37)$$

Triangle basis functions, $t_n(s; s_{n-1}, s_n, s_{n+1})$, are shown in Figure 5.8(a). They are applied to the cylindrical scatterer geometry, to approximate the transverse current density in Equation 5.38, shown in Figure 5.7.

$$J_t(r) = \sum_{n=1}^N b_n t_n(s; s_{n-1}, s_n, s_{n+1}) \quad (5.38)$$

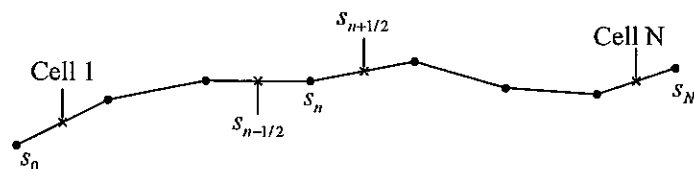


Figure 5.7 Segmentation of cylindrical scattering section used for defining the basis functions.

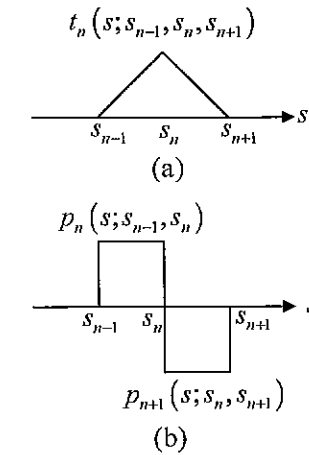


Figure 5.8 (a) Triangle basis function, $t_n(s; s_{n-1}, s_n, s_{n+1})$, used for the transverse surface current, J_t . (b) Equivalent pulse basis functions $p_n(s; s_{n-1}, s_n)$ and $p_{n+1}(s; s_n, s_{n+1})$ used for the surface charge density, ρ_e .

The surface charge density can be represented by a combination of two pulse basis functions, shown in Figure 5.8(b), which is consistent with the equivalent representation of triangle basis function for J_t , and can be given by:

$$\rho_e(r) = \frac{j}{\omega} \sum_{n=1}^N b_n \left(\frac{1}{s_n - s_{n-1}} p_n(s; s_{n-1}, s_n) - \frac{1}{s_{n+1} - s_n} p_{n+1}(s; s_n, s_{n+1}) \right) \quad (5.39)$$

A reason for the selection of pulse basis functions for the surface charge density is because it enables the application of the identity in Equation 5.40, for a simplified treatment of the gradient operator on Φ_e .

$$\int p(s; s_1, s_2) \hat{t}(\rho) \cdot \nabla F ds = \int_{s_1}^{s_2} \frac{dF}{ds} ds = F(s_2) - F(s_1) \quad (5.40)$$

Equations 5.38 and 5.39 are substituted into Equations 5.35 and 5.36 for A and Φ_e , which are then substituted into the EFIE in Equation 5.34 to obtain an expression for the unknown transverse surface current, b_n .

The EFIE is enforced by pulse testing functions in a point-matching approach, which involves multiplying both sides of the Equation using a testing function and integrating over the scatterer surface. The pulse testing functions spanning over the midpoints of adjacent strips are given by:

$$T_m(r) = p_n(s; s_{m-1/2}, s_{m+1/2}) \quad (5.41)$$

Dividing the scatterer geometry into cells enables this EFIE to be expressed as an $N \times N$ system of linear equations. Equation 5.42 is solved to obtain the surface current corresponding to the position of the cell on the scatterer.

$$\begin{bmatrix} e_1 \\ e_2 \\ e_3 \\ \vdots \\ e_N \end{bmatrix} = \begin{bmatrix} Z_{11} & Z_{12} & Z_{13} & \cdots & Z_{1N} \\ Z_{21} & Z_{22} & Z_{23} & \cdots & Z_{2N} \\ Z_{31} & Z_{32} & Z_{33} & \cdots & Z_{3N} \\ \vdots & \vdots & \vdots & \ddots & \vdots \\ Z_{N1} & Z_{N2} & Z_{N3} & \cdots & Z_{NN} \end{bmatrix} \begin{bmatrix} b_1 \\ b_2 \\ b_3 \\ \vdots \\ b_N \end{bmatrix} \quad (5.42)$$

where the incident electric field values are given by:

$$e_m = \int_{s_{m-1/2}}^{s_{m+1/2}} \hat{t}(r) \cdot E^{inc}(r) ds \quad (5.43)$$

The impedance matrix values are calculated from:

$$\begin{aligned} Z_{mn} = & \frac{k\eta}{4} \int_{s_{m-1/2}}^{s_{m+1/2}} \hat{t}(r) \cdot \left[\int_{s_{n-1}}^{s_{n+1}} \hat{t}(r') t(r'; t_{n-1}, t_n, t_{n+1}) H_0^{(2)}(kR_1) ds' \right] ds \\ & + \frac{\eta}{4k} \left(\frac{1}{s_n - s_{n-1}} \int_{s_{n-1}}^{s_n} H_0^{(2)}(kR_2) ds' - \frac{1}{s_{n+1} - s_n} \int_{s_n}^{s_{n+1}} H_0^{(2)}(kR_2) ds' \right. \\ & \left. - \frac{1}{s_n - s_{n-1}} \int_{s_{n-1}}^{s_n} H_0^{(2)}(kR_1) ds' - \frac{1}{s_{n+1} - s_n} \int_{s_n}^{s_{n+1}} H_0^{(2)}(kR_1) ds' \right) \end{aligned} \quad (5.44)$$

where:

$$R_1 = \sqrt{\left[x(s_{m-1/2}) - r'_x \right]^2 + \left[y(s_{m-1/2}) - r'_y \right]^2} \quad (5.45)$$

$$R_2 = \sqrt{\left[x(s_{m+1/2}) - r'_x \right]^2 + \left[y(s_{m+1/2}) - r'_y \right]^2} \quad (5.46)$$

5.4 Scattering Program Description

Two scattering programs were used to solve for the TM and TE components. A description of the general methodology used to obtain the reflector patterns follows.

The Cartesian equation for the transverse profile of the cylindrical reflector geometry, with a known focal length f , centred with its vertex at the origin is:

$$y^2 = 4fx \quad (5.47)$$

This can be modified to give:

$$y^2 = -\frac{1}{f} \left(\frac{D}{2} \right)^2 x + \left(\frac{D}{2} \right)^2 \quad (5.48)$$

Equation 5.48 is used in the analysis because it positions the focal point of the cylindrical reflector at the origin and shows a dependence on the aperture diameter D . It also provides flexibility to generate (x, y) points to represent reflectors with different f/D .

The points that describe the reflector in Figure 5.9 are obtained by specifying a step size, Δd , in the positive y -direction. A set of y -points are generated across a specified range: $[0, D/2]$, spaced by Δd :

$$\begin{aligned} y(1) &= 0 \\ y(n+1) &= y(n) + \Delta d \quad \text{for } n = 1 \rightarrow D/\Delta d \end{aligned} \quad (5.49)$$

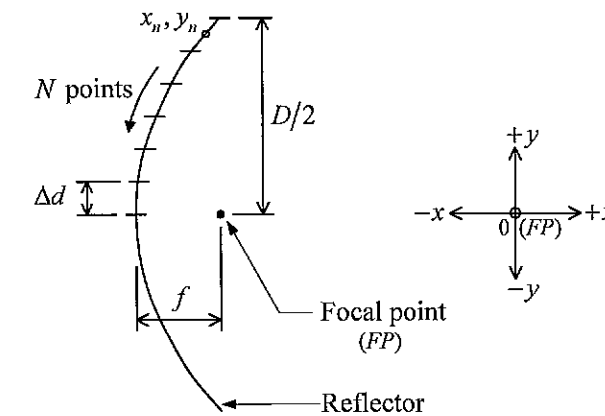


Figure 5.9 Representation of the cylindrical reflector in the transverse plane using Cartesian geometry.

The number of points is determined by the Δd spacing in the y -direction and the maximum number of points is $N = D/\Delta d$. Corresponding values for the points in the x -direction can be calculated by Equation 5.48. The complete description of the reflector is obtained by also generating points in the negative y -direction: $[-D/2, 0]$. The coordinate points are input to the scatterer program. Arbitrary cylindrical scattering sections, such as ground planes and support struts, can be included in the model by generating a set of coordinates that correspond to their geometry. Once reflector points are read by the program, a segmentation routine generates a set of cells with a specified width and corresponding unit vectors and midpoints to describe the reflector geometry. The number of cells used to model the reflector is adjusted by modifying an input parameter representing the cell width. An increased number of cells provide a better representation of the reflector profile, improving the accuracy of the solution. However, the penalty is an increase in computational complexity when solving Equations 5.31 and 5.42.

After the reflector geometry has been divided into cells, a feed model that will be described in Section 5.5 is used to generate the incident field on the reflector. Point matching is used, where the incident field is calculated at the midpoint of each cell to generate an excitation or voltage vector $[V_{inc}]$. An impedance matrix $[Z]$ is generated by using Equations 5.29 and 5.33 for the TM polarisation and Equation 5.44 for the TE polarisation. The current vector $[J]$, describing the surface current at midpoints of the cells on the reflector, is obtained by solving the system of equations: $[Z][J] = [V_{inc}]$ using lower-upper decomposition and back substitution. After obtaining the surface currents, the total far-field reflector pattern is generated by summing the incident field and the field due to the reflector surface currents. From this pattern, parameters such as the half-

power beamwidth, sidelobe level, gain in the transverse plane and reflector noise temperature are obtained. The feed model can be adjusted to generate incident fields with varying beamwidths in order to determine the transverse feed pattern that will provide optimum sensitivity (A_{eff}/T).

Adjusting the feed model position in relation to the focal point enables investigation of defocusing effects and comparison of the two line feed solutions described in Section 3.4. Line feed blockage is modelled by including points for the scatterer geometry that represent the line feed ground plane profile. The standing wave cavity effect generated between the cylindrical reflector vertex and ground plane can be studied and is described in Section 5.6.4. The accuracy of the program was checked by modelling and comparing results with structures in Andreassen (1964) which had a known surface current distribution and far-field pattern when excited by an incident plane wave for TM and TE polarisations. Approximations were used to calculate some of the impedance matrix entries that described self-terms (Z_{nn}) for the TM analysis due to an integrable singularity in the Green's function. This approximation was used because it facilitates a simpler calculation.

Mutual coupling between line feed elements and scanning effects are not included in either TM or TE models, as it would lead to inefficient optimisation of the feed. Mutual coupling effects occur in the far-field region of the reflector and are included in the scan element pattern, described in Chapter 6. Scanning effects are also assumed in the element pattern and an investigation into reflector pattern performance with scan angle for the new line feed design is presented in Chapter 8. The accuracy of the solution for the surface currents is limited by the computing memory required. The reflector surface at the MOST was constructed around 1960 and effects such as reflector profile distortion may limit the agreement between simulated and measured reflector pattern performance.

5.5 Feed Model

A feed model representing the field incident on the reflector is required, so the excitation vector can be defined for the method of moments formulation in Equations 5.31 and 5.42. The model must be flexible and generate feed patterns with varying half-power beamwidths to enable the investigation of a feed beamwidth that provides optimum sensitivity.

The model uses a current point source located in the focal region. For the TM component an electric point source is used, whereas a magnetic point source (Section 5.3) was used for the TE component. Point current sources are used in the feed model rather than transverse current sources, because they are z -directed with no direction vector to be specified over a particular length. This enabled greater flexibility and simplicity in generating the required feed pattern beamwidths. Although a transverse electric current, J_t , was depicted as the TE source in Figure 5.1(b), it can be represented by an equivalent z -directed magnetic current source, K_z by the principle of duality (Harrington 1961). A ground plane was placed behind the source to provide directional radiation and model blockage, as depicted in Figure 5.10. The feed pattern beamwidth can be varied by adjusting the position and number of the current sources placed above the ground plane. For narrower beamwidths, several current sources can be arrayed in the transverse

direction above the ground plane. Furthermore, the amplitude and phases of the arrayed sources can be adjusted to shape the feed pattern. In this analysis, the feed model was adjusted to produce beamwidths ranging from 50° – 120° , typical of beamwidths for the feed elements listed in Table 4.1. The upper limit of the beamwidth, 120° , was selected to be large because the MOST reflector has a deep profile, which requires a large beamwidth for efficient illumination.

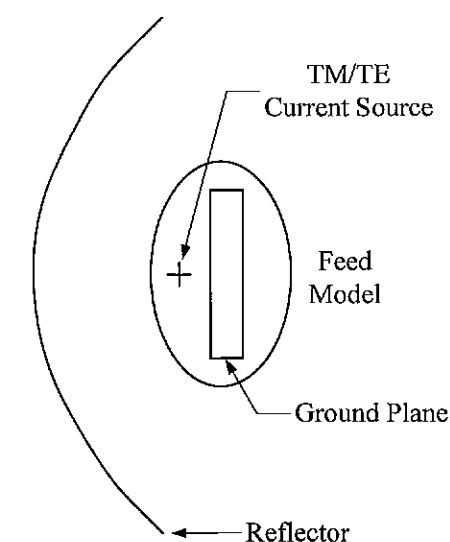


Figure 5.10 Feed model (not to scale), with current source above a ground plane to generate the transverse feed pattern for the combined reflector and feed model.

The width of the transverse ground plane was set to 500 mm, which is the width of the current line feed ground plane. This parameter is fixed to enable the use of existing feed support struts. However, this width is not ideal for wide frequency operation because it does not allow the minimisation of blockage effects at lower frequencies where the electrical size of the reflector becomes small. Cross-polar radiation patterns are either TM or TE components depending on the feed polarisation, as shown in Table 5.1. However, cross-polar patterns are specific to the type of element used. After the measured line feed polarisation performance has been presented in Chapter 7, the reflector polarisation will be modelled and is described in Chapter 8.

5.5.1 Feed Illumination Patterns

The bandwidth for the line feed, in Section 4.3, was specified as 1.7:1 in the range 500–1000 MHz. The simulations in Section 5.6 are only carried out at the centre frequency, 866 MHz, except for the wideband performance investigation in Section 5.6.4. Because of the electric field alignment of the source on the ground plane, the TM and TE components produce different radiation patterns. For purposes of the feed pattern investigation, the co-polar TM component is used because it is not significantly affected by the finite edge effects of the ground plane, compared to the TE component. Edge effects are reduced in the TM case because the scattered electric fields are aligned in the z -direction and 'see' a continuous environment rather than a finite edge. Minimisation of these edge effects for the co-polar TE component is investigated in Section 5.6.3.

In the feed model, the height of the source above the ground plane is 0.25λ at the centre frequency, to accommodate the balun feeding arrangement planned for the initial wideband dipole prototype. This height ensures that the phase centre of the feed model remains within the same region as the dipole prototype. Feed models for beamwidths ranging from 50° – 100° used two sources spaced symmetrically about the centre of the ground plane with the spacing modified for beamwidth adjustment. For feed models with beamwidths $> 100^\circ$, a single source is needed and its height above the ground plane increased to broaden the beamwidth. The maximum height above the ground plane was 0.3λ for the 120° beamwidth model.

Feed model patterns for beamwidths in the 50° – 120° range are shown in Figure 5.11. A comparison of these beamwidths for different reflector performance parameters is presented in Table 5.2. The edge taper describes the gain of the pattern at the reflector edge compared to its maximum gain, as shown in Figure 3.3. Spillover and taper efficiencies are calculated respectively from Equations 3.5 and 3.4. Spillover temperature is calculated using Equation 3.13. Aperture efficiency is calculated using Equation 3.2, assuming a polarisation efficiency equal to 1 and a constant blockage efficiency of 0.92 (from Equation 3.7). As expected, edge taper levels increase with beamwidth. Spillover efficiency is higher at smaller beamwidths because a larger portion of the pattern is captured by the reflector. Conversely, the taper efficiency is lower at smaller beamwidths because the pattern illuminates less of the reflector. Figure 5.11 shows sidelobes appearing in the 50° beamwidth pattern, which is characteristic of narrow-beamwidth patterns. The edge taper value for this beamwidth is misleading because the sidelobe coincides with the reflector subtended half-angle ($\pm 88^\circ$) value rather than at the main beam of the feed pattern. Although feed patterns with narrow beamwidths, $< 70^\circ$, have high spillover efficiency, the low taper efficiency limits the aperture efficiency to < 0.4 .

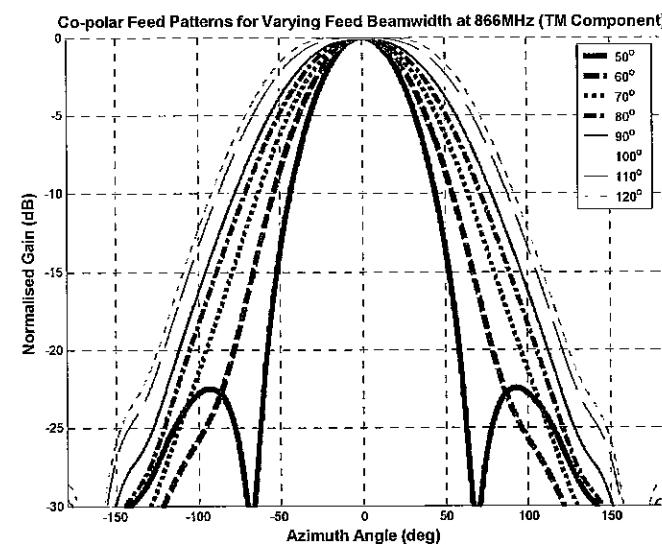


Figure 5.11 Co-polar TM feed patterns for varying feed beamwidths at 866 MHz.

Feed HPBW ($^\circ$)	Edge Taper (dB)	Spillover eff (η_{sp})	Taper eff (η_t)	Aperture eff (η_{ap})	Spill temp (K)
50	-23	0.99	0.27	0.27	3.1
60	-23	0.99	0.35	0.35	3.1
70	-18	0.99	0.43	0.43	3.3
80	-15	0.99	0.48	0.48	3.5
90	-13	0.98	0.51	0.50	3.7
100	-11	0.98	0.53	0.52	3.8
110	-10	0.97	0.56	0.54	4.0
120	-9	0.97	0.61	0.59	4.2

Table 5.2 Comparison of simulated performance for MOST over a range of practical beamwidths.

Figure 5.12 shows a plot of spillover, taper and aperture efficiencies for varying beamwidths. This figure shows the trade-off between low spillover and high taper efficiency. The deep taper of the MOST reflector ($f/D = 0.26$) was chosen to minimise spillover temperature for low noise operation, but as a consequence low taper efficiencies result. A feed with a beamwidth over 100° would provide a reasonable taper efficiency. However, the spillover temperature increases, which compromises the telescope sensitivity. Improving the aperture efficiency by increasing the feed beamwidth beyond 100° is not practical over a wide bandwidth using the types of elements considered in Table 4.1. A feed beamwidth range of 70° – 100° , corresponding to an edge taper range of -18 to -11 dB was selected for the design. This range will produce spillover efficiencies of 0.98–0.99, spillover temperatures of 3.3–3.8 K, taper efficiencies of 0.43–0.53 and aperture efficiencies of 0.43–0.52. Although the aperture efficiency range is slightly less than the 0.5 design specification, presented in Section 3.3.1, a minimum spillover temperature is important for telescope sensitivity. Furthermore, based on the scanning performance of line feeds in other cylindrical reflector systems described in Section 3.3.2, it is anticipated that the antenna temperature will rise when the scan angle is increased. The aperture efficiency may fall below the 0.43 value at large scan angles. The variation of aperture efficiency with scan angle for the wideband line feed prototype is presented in Section 7.3.

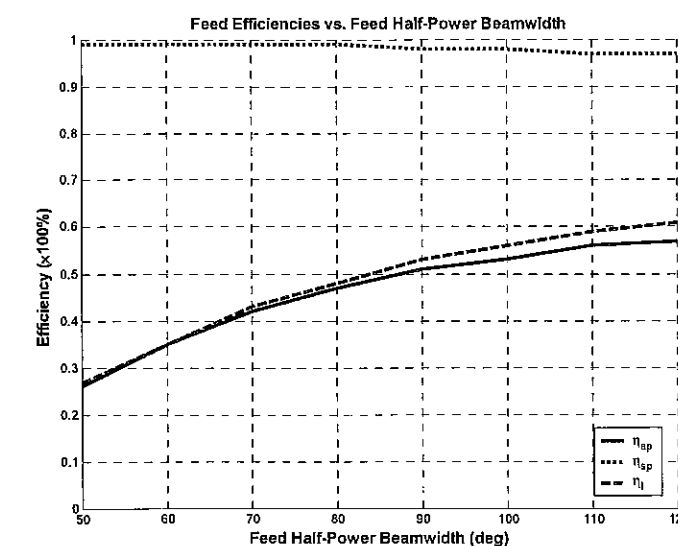


Figure 5.12 Aperture (η_{ap}), spillover (η_{sp}) and taper (η_t) efficiencies as a function of feed beamwidth.

5.6 Combined Feed and Reflector Model Simulations

In Section 5.5, a feed model was developed which could be adjusted to produce patterns with varying beamwidths. This was used to select the beamwidth range for optimum telescope sensitivity. In this section, the feed model is combined with the cylindrical reflector in the method of moments simulation to produce the reflector pattern.

5.6.1 Focal Region Analysis

A focal plane analysis determines the phase centre of the reflector and evaluates the feasibility of the two line feed solutions described in Section 4.3. Two directions of focal plane displacement are considered: displacement along the focal line or x -axis, in Figure 5.13(a) and displacement along the aperture or y -axis, in Figure 5.13(b). In this analysis a TM co-polar 80° beamwidth feed model (Section 5.5.1) will be used, with simulations carried out at the centre frequency, 866 MHz.

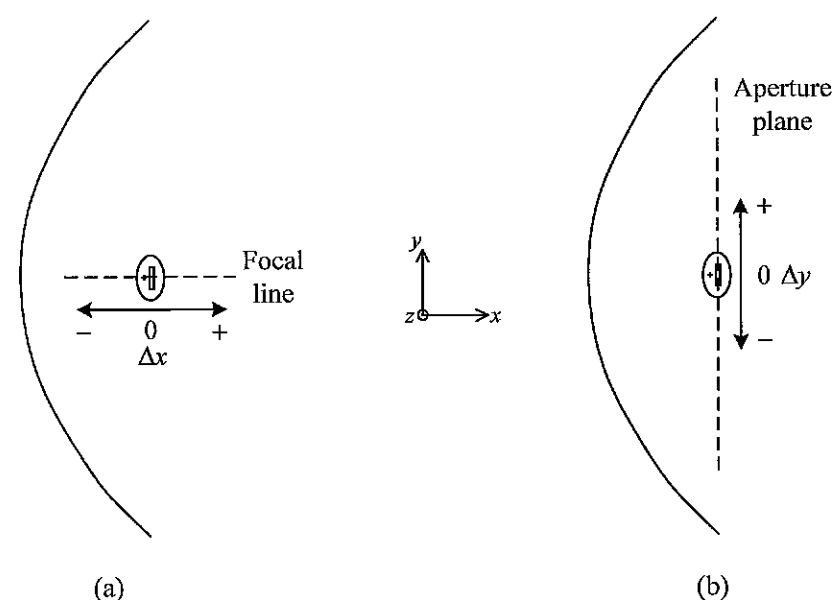


Figure 5.13 Displacement in the focal plane. (a) Along the focal line or x -axis. (b) Along the aperture plane or y -axis.

Feed displacement in the x -axis is used to determine the phase centre of the reflector, which is the reference point that maximises reflector efficiency and produces maximum directivity. Initially an approximate phase centre is estimated. Consider a current source above an infinite ground plane. From image theory (Harrington 1961), the radiation pattern can be represented by two image currents with the same magnitude and spaced at a distance being twice the height of the source above the ground plane. The phase centre occurs at the midpoint between the two image currents, which corresponds to the surface of the ground plane. For a finite ground plane, the phase centre is not exactly at the surface of the ground plane. This shift is caused by additional ground plane edge currents, which cause diffraction and contribute to the radiation pattern. As a result, the point halfway between the source and the ground plane is chosen as the reference position for the analysis, as shown in Figure 5.14.

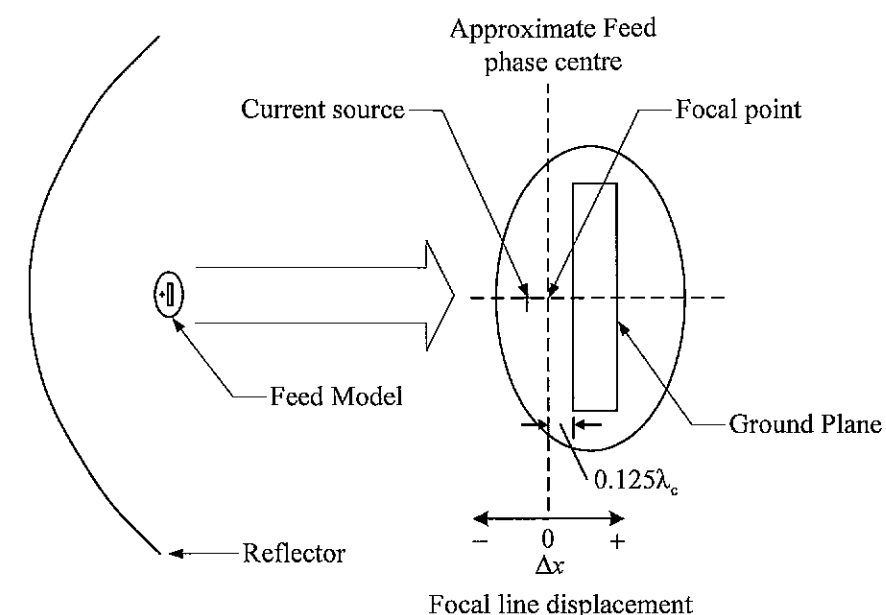


Figure 5.14 Focal plane displacement along the x -axis, showing the approximate feed phase centre as the reference point.

In the analysis, the selected reference point is aligned with the focal point of the reflector and then displaced at 0.05λ intervals in the x -axis. Results for reflector performance at points along the x -axis in the region between $\pm 0.2\lambda$ are shown in Table 5.3. The gain was calculated in the transverse plane for a 360° angular region and the noise temperature in the reflector pattern is calculated using Equation 3.15.

Δx (λ)	Reflector HPBW ($^\circ$)	Sidelobe Level (dB)	Gain (dB)	Reflector Temp (K)
-0.20*	2.5	-18.0	18.0	3.0
-0.15*	2.1	-19.0	19.0	3.1
-0.10	1.9	-17.5	19.5	3.2
-0.05	1.8	-17.0	20.0	3.4
0.00	1.8	-17.0	20.0	3.5
+0.05	1.8	-18.0	20.0	3.6
+0.10	1.8	-20.0	20.0	3.7
+0.15*	1.8	-20.0	19.5	3.7
+0.20*	2.0	-18.0	19.0	3.5

Table 5.3 Comparison of co-polar TM reflector patterns for focal region displacements along the x -axis, with an 80° HPBW feed at 866 MHz. * Denotes defocused positions.

Normalised gain and sidelobe levels for a varying x -directed feed position are seen respectively in Figures 5.15(a) and 5.15(b). Figure 5.15(a) shows the reflector phase centre occurs at a displacement around 0 to $+0.05\lambda$. Some sidelobe levels shown in Figure 5.15(b) are misleading. When the feed model is displaced by more than 0.1λ from the focal point, the reflector pattern becomes defocused and exhibits null-filling between sidelobes. Null-fill is caused by the aperture blockage of the ground plane and varies as the feed is displaced because there is a standing wave between the reflector vertex and ground plane, which adds either constructively or destructively to the gain. Displacements denoted by an asterisk (*) in Table 5.3 indicate the pattern is defocused and exhibits null-fill. The reflector temperature generally increases as the feed is

displaced away from the vertex, as more of the feed pattern 'spills over' at the reflector edges.

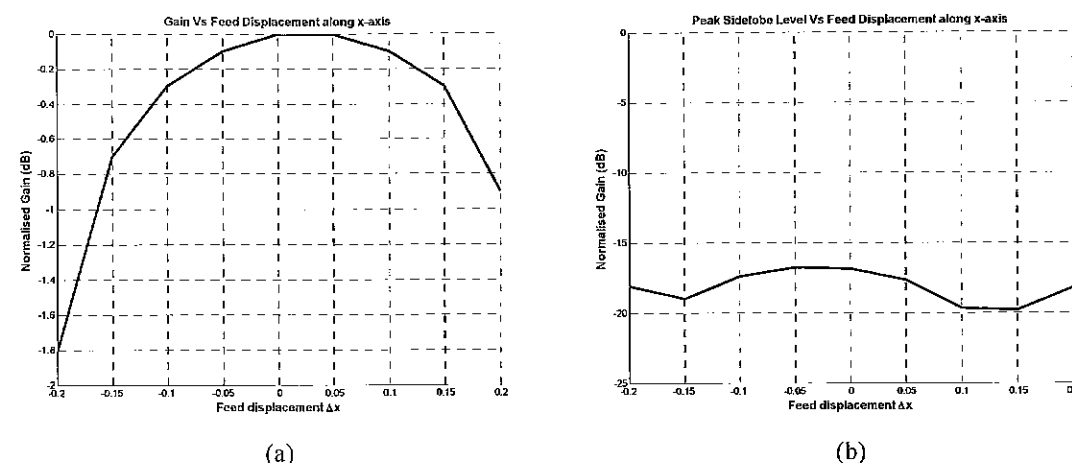


Figure 5.15 Variation in the reflector pattern due to x-directed focal region displacement. (a) Normalised gain. (b) Sidelobe level.

Reflector patterns for x-directed focal displacements at $\pm 0.2\lambda$ and 0.0λ are shown in Figure 5.16. Displacements at $\pm 0.2\lambda$ show the effects of null-filling and defocusing due to the ground plane blockage. When the feed is displaced towards the reflector vertex, i.e. the $-x$ -direction, there is a gain reduction because the feed edge taper is increased. The antenna temperature decreases because more feed radiation is captured by reflector. When the feed is moved away from the reflector vertex, i.e. the $+x$ -direction, the gain reduces because more feed radiation is being directed into spillover regions and appear in the form of higher sidelobes in the reflector region. In both cases where the feed is moved away from the focal point, there is a non-uniform sidelobe taper which is due to the ground plane blockage. The focal region size for which there is a uniform sidelobe taper and no null-fill defocusing effects is from -0.1λ to $+0.1\lambda$ about the focal point. Subsequent reflector simulations will use no focal plane x-displacement ($\Delta x = 0\lambda$) for the phase centre reference point.

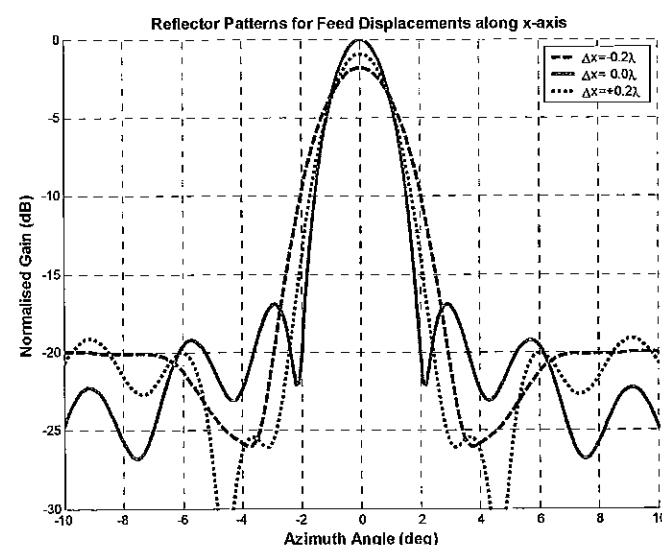


Figure 5.16 Reflector patterns for several x-directed displacements.

Focal plane displacement of the feed model along the aperture, or in the y -direction, is shown in Figure 5.17. The feed model is aligned with the y -axis at the reflector vertex and the feed phase centre determined from the x -directed focal plane displacement is used for the investigation. The feed is then displaced in 0.05λ intervals along the y -axis within the $\pm 0.2\lambda$ range. This analysis of displacing the feed along the aperture evaluates the configuration proposed in the contiguous multi-line feed solution described in Section 4.3.

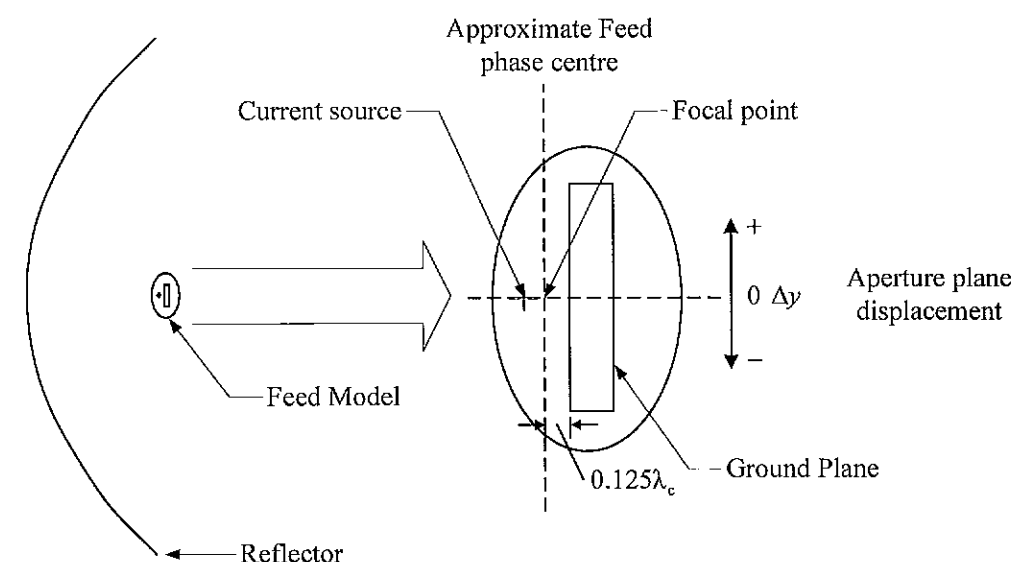


Figure 5.17 Focal plane displacement along the y -axis, showing the reference point for the aperture plane displacement.

Results for pattern parameters due to the displacement in the y -direction are shown in Table 5.4. As the feed is displaced in this direction, the beam centre shifts away from boresight (0°) and there is a slight gain decrease and an increase in sidelobe levels as shown in Figure 5.18. Normalised gain and sidelobe levels for a displacement in the y -direction are shown respectively in Figures 5.19(a) and 5.19(b). There is a minimal gain variation when the feed model is displaced, because the displacement is not large enough to produce a large change in reflector illumination. Similarly there is a minimal change in reflector temperature because most of the radiation occurs in the forward angular direction (within $\pm 90^\circ$) and outside this range the radiation is below -40 dB. Increased sidelobes due to feed displacement shown in Figure 5.18 are called coma sidelobes and occur asymmetrically. Defocusing effects occur as the feed is moved off axis in the y -direction. The acceptable sidelobe level in the reflector pattern is not specified in Table 3.6, since this changes for different science goals. However, minimisation of sidelobe levels is desirable from a noise performance viewpoint. Although the maximum sidelobe level for the current MOST imaging beam is around -10 dB, a uniform reflector illumination has a maximum sidelobe level around -13 dB, which will be the value used as the acceptable level. Using this specification, the focal region in the y -direction is acceptable within $\pm 0.15\lambda$ of the focal point.

Δy (λ)	Reflector HPBW ($^\circ$)	Beam Centre ($^\circ$)	Sidelobe Level (dB)	Gain (dB)	Reflector Temp (K)
-0.20	1.8	+0.9	-12.0	19.9	3.5
-0.15	1.8	+0.7	-13.5	19.9	3.5
-0.10	1.8	+0.5	-14.5	19.9	3.5
-0.05	1.8	+0.2	-15.5	20.0	3.5
0.00	1.8	0.0	-17.0	20.0	3.5
+0.05	1.8	-0.2	-15.5	20.0	3.5
+0.10	1.8	-0.5	-14.5	19.9	3.5
+0.15	1.8	-0.7	-13.0	19.9	3.5
+0.20	1.8	-0.9	-12.0	19.9	3.5

Table 5.4 Comparison of reflector patterns for different y -directed displacements in the focal plane.

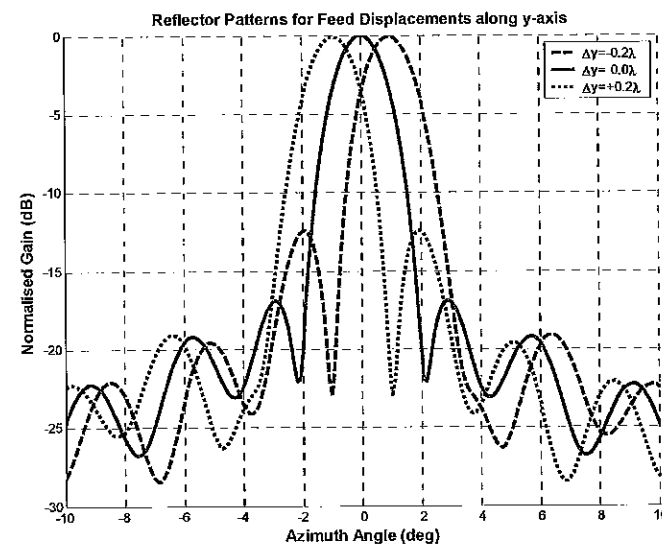


Figure 5.18 Reflector patterns for several y -directed feed model displacements.

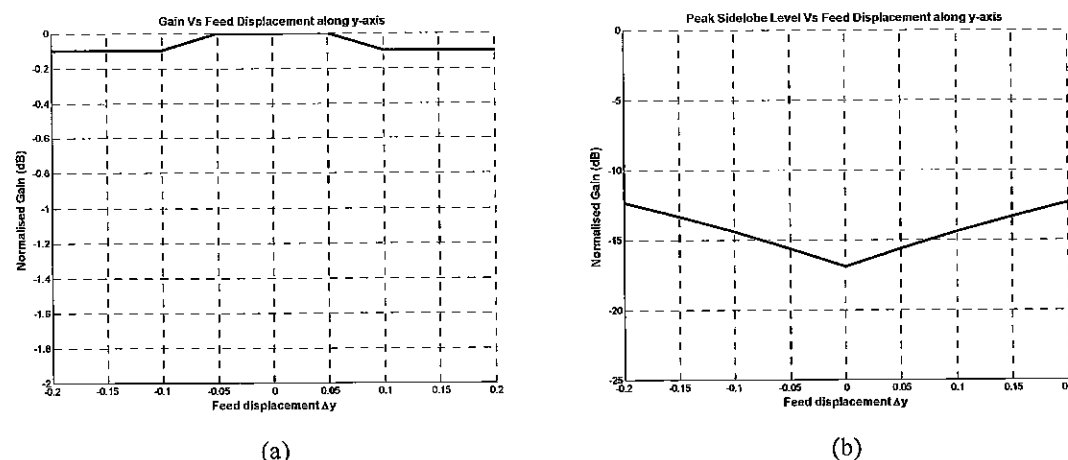


Figure 5.19 Variation in the reflector pattern due to y -directed focal region displacement. (a) Normalised gain. (b) Sidelobe level.

The multi-band contiguous line feed solution described in Section 4.3 requires some feeds to be offset in the y -direction. Figure 5.18 shows pattern defocusing effects occur when the feeds are offset. A larger ground plane width in the y -direction is required for the additional feeds, which increases the feed blockage and reduces aperture efficiency. Coupling between multiple line feed bands is higher compared to a rotating turret

configuration. Line feeds on the turret are placed on separate ground planes with a greater physical separation between bands. Advantages of the contiguous configuration are: no moving mechanical parts and simultaneous operation of different bands. Simultaneous operation improves the observing efficiency when the telescope is used for survey observations. A rotating turret configuration allows each line feed band to be placed in the centre of the ground plane. This minimises defocusing effects and creates symmetrical patterns because each feed remains fixed at the reflector phase centre, with no offset in the y -direction. On balance, the rotating turret configuration is preferred because of minimal defocusing effects.

5.6.2 Reflector Pattern Analysis

Although the ideal feed HPBW range, 70° – 100° , was determined in Section 5.5.1, this analysis did not consider the reflector pattern performance. This section investigates this performance across the range of practical feed beamwidths, 50° – 120° . The reflector phase centre determined in Section 5.6.1 is used as the feed placement point and simulations are carried out at 866 MHz, with 10 cells per wavelength to represent the reflector and ground plane.

Reflector pattern performance parameters across the practical feed beamwidth range are shown in Table 5.5. The gain was calculated in the transverse plane for a 360° angular region and the noise temperature in the reflector pattern was calculated using Equation 3.15. An estimate of the sensitivity parameter, A_{eff}/T , is given. The effective area, A_{eff} , is determined using Equation 3.1, by assuming a physical aperture area of $18,000 \text{ m}^2$ and the aperture efficiency from Table 5.2. The noise temperature, T , is from radiation characteristics of the line feed and determined by either the spillover temperature in Table 5.2 or reflector temperature in Table 5.5. Other temperature contributions such as feed loss and receiver noise are independent of the line feed radiation.

Feed HPBW ($^\circ$)	Reflector HPBW ($^\circ$)	Sidelobe level (dB)	Gain (dB)	Reflector Temp (K)	A_{eff}/T (m^2/K)
50	2.7	-17.0	17.5	3.4	650
60	2.0	-19.0	19.0	3.3	1,800
70	1.9	-19.0	19.5	3.4	2,000
80	1.8	-17.0	20.0	3.5	2,100
90	1.7	-15.5	20.0	3.6	2,050
100	1.7	-14.5	20.0	3.7	2,000
110	1.7	-14.0	20.0	3.7	2,000
120	1.6	-13.0	20.0	3.9	2,000

Table 5.5 Comparison of co-polar TM reflector pattern parameters for different feed beamwidths at 866 MHz.

Table 5.5 shows that when the feed beamwidth is increased, the reflector pattern beamwidth decreases, and sidelobe levels, gain and reflector temperature increase. This is expected because larger feed beamwidths have a smaller edge taper corresponding to increased illumination across the reflector. Reflector noise temperatures are within 0.3 K of the corresponding spillover temperature calculations listed in Table 5.2. This agreement means that the noise temperature is dominated by the line feed pattern rather than the reflector. Therefore, the spillover temperature can be used for the sensitivity

calculation. Estimated sensitivities for the feed radiation in the selected beamwidth range, 70° – 100° , are relatively uniform and are around $2,000 \text{ m}^2/\text{K}$. Although good sensitivity is achievable for feed beamwidths above 100° , other factors such as increased sidelobe levels and spillover temperature are limiting factors. The improvement in sensitivity for large feed beamwidths is due to the increased taper efficiency, resulting in increased aperture efficiency.

Reflector patterns for feed beamwidths of 60° , 80° and 100° are shown in Figures 5.20 to 5.22. These patterns show a main beam flanked by decreasing inner sidelobe levels, but with sidelobes then increasing at angles corresponding to the reflector edge ($\pm 88^\circ$). Further out there is a sharp drop in sidelobe levels. The increase in sidelobe levels near the reflector edges represents the spillover contribution from the feed pattern. This contribution is reduced for feed patterns with a larger edge taper, as seen by comparing the angular region around $\pm 88^\circ$ for a 60° beamwidth feed in Figure 5.20 with a 100° feed in Figure 5.22. The abrupt drop in gain at the reflector edge represents a scattering phenomenon known as edge diffraction. The gain in the angular region behind the reflector, outside the subtended half angle region $\pm 88^\circ$, is quite low because the ground plane directs most of the radiation towards the reflector.

The pattern for a perfectly focused reflector has deep nulls between successive sidelobes, whereas the presence of null-fill indicates a phase error due to defocusing. Although the feed model is placed at the reflector phase centre, there is a slight defocusing effect for reflector patterns with feed beamwidths $< 70^\circ$, highlighted by greater null-fill between sidelobes compared to patterns with larger feed beamwidths. These phase errors occur at smaller feed beamwidths with large edge tapers since the reflector is not as uniformly illuminated as a feed with a smaller edge taper. Furthermore, the ground plane blockage contributes to the defocusing effects causing phase errors in the sidelobes. Figure 5.22 shows null-fill is less for a 100° feed than for the 60° feed (Figure 5.20). The symmetric feed configuration of the MOST causes a standing wave between the reflector vertex and feed ground plane. When the operating frequency changes, the frequency of the standing wave also changes which can cause defocusing and gain variation. This effect is investigated in the wideband reflector analysis described in Section 5.6.4.

The analysis of the reflector patterns across the practical feed beamwidth range, confirms that a beamwidth in the range from 70° – 100° is viable. Reflector patterns for feed beamwidths below 70° exhibited excessive phase errors shown by increased null-fill, whereas feed beamwidths above 100° have increased noise temperature and sidelobe levels to around -13 dB .

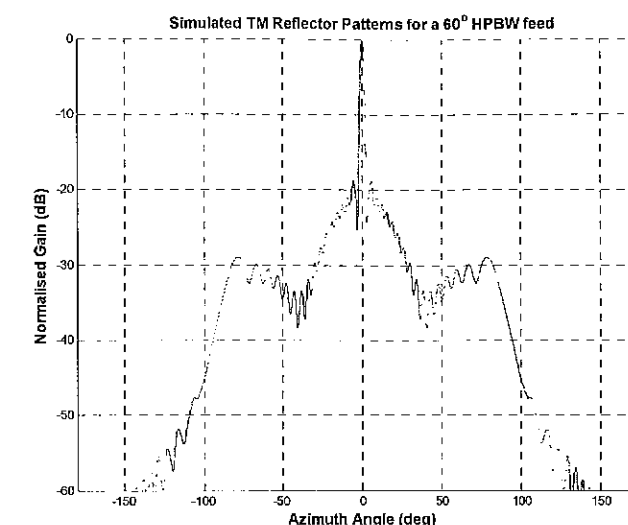


Figure 5.20 Simulated reflector patterns for the MOST, illuminated by a 60° HPBW model.

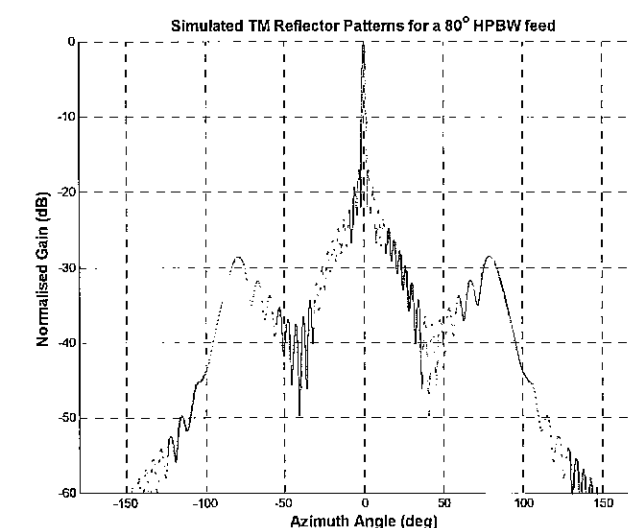


Figure 5.21 Simulated reflector patterns for the MOST, illuminated by an 80° HPBW model.

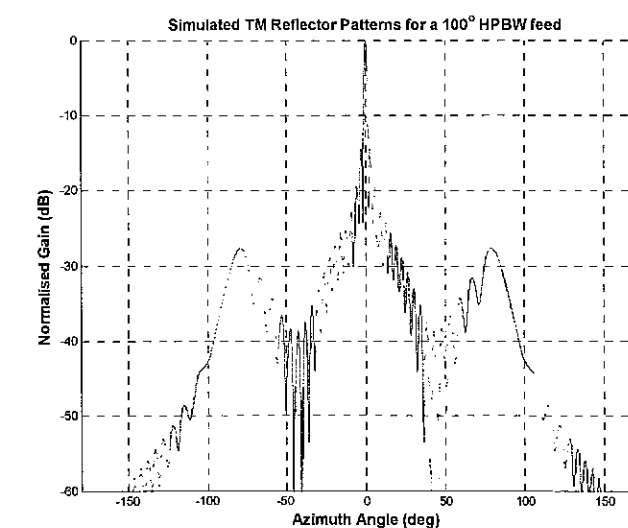


Figure 5.22 Simulated reflector patterns for the MOST, illuminated by a 100° HPBW model.

5.6.3 Beamwidth Matching

Simulations for the TM component of the electromagnetic field were carried out for the feed and reflector in Sections 5.6.1 and 5.6.2. However, a feed model is also required for the TE component to model the horizontal co-polar and vertical cross-polar patterns, as listed in Table 5.1. This will complete the solution for the electromagnetic fields presented in Equation 5.4. TE analysis has been deferred until now because of difficulty in generating a feed pattern with an arbitrary beamwidth. This difficulty arises because the scattered field in the TE case occurs along the reflector surface, in a direction transverse to the z -direction. When the incident field from a current source encounters a 'finite edge', such as the edge of a ground plane, diffraction occurs and edge currents are generated. These edge currents cause pattern degradation because their polarisation orientation differs from the incident current source. The incident z -directed field in the TM analysis generates scattered z -directed currents, so the polarisation orientation remains the same and finite edge effects are reduced. This means the TM feed model using point sources above the ground plane is more flexible in controlling the feed beamwidth.

In the TE feed model a similar approach was adopted. Magnetic point sources were placed above a ground plane and their positions were adjusted to modify the feed beamwidth. To evaluate the model, the radiation from a horizontally polarised dipole was represented by equivalent magnetic sources. Two magnetic sources were spaced approximately 0.5λ apart at the centre frequency and positioned about the centre of the ground plane. The height of the sources above the ground plane was initially set at 0.25λ , but was reduced to produce directional radiation. To verify the TE feed modelling, a horizontally polarised dipole was simulated using commercially available 3D EM solver software, CST Microwave Studio (MWS). A description of this software is presented in Section 6.2. Results in Figure 5.23 show good agreement between the TE feed model using point sources and an equivalent simulated CST MWS horizontally polarised dipole.

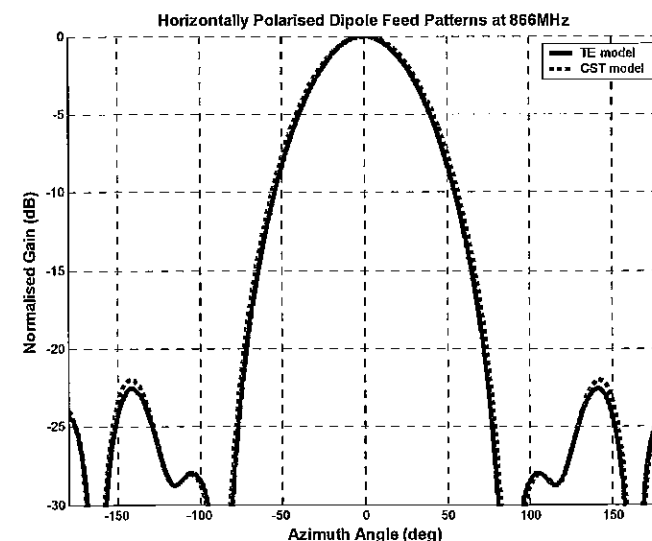


Figure 5.23 Comparison of the TE feed model with an equivalent CST MWS simulation for a horizontally polarised dipole at 866 MHz.

Although the TE model could be used to generate patterns to represent a horizontally polarised dipole, feed patterns like those produced using the TM feed model could not be generated. This was because dual linear polarisation was used for the line feed (Section 3.3.4), which produces unequal radiation for co-polar TE and TM components. SKAMP is specified with equal co-polar beamwidths for both polarisations. A limitation in the TE feed model comes from the edge currents produced by the finite ground plane. A technique to minimise these effects and improve the beamwidth match with the TM feed model, involved placing two channels either side of the current sources positioned symmetrically about the centre of the ground plane as shown in Figure 5.24.

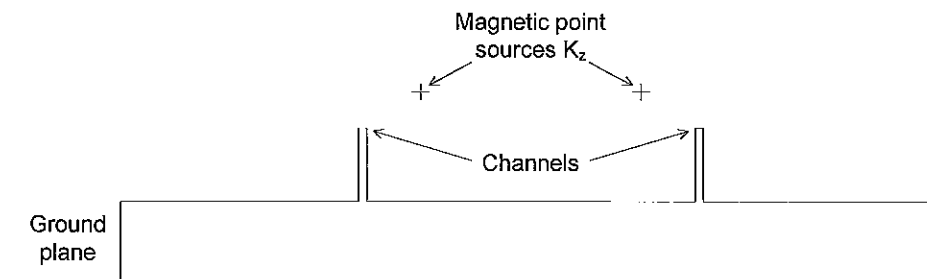


Figure 5.24 TE feed model, with channels to minimise edge currents from the finite ground plane edge and to improve the co-polar beamwidth match with the TM model.

Channel dimensions that minimised ground plane effects and provided the best beamwidth matching at the centre frequency, were 200 mm wide and 45 mm high. A parameter analysis to determine the optimum beamwidth is described in Section 6.4.2. To demonstrate this technique, simulations were conducted for the TM and TE models, at the centre frequency, to match the beamwidths to an 80° feed beamwidth pattern as shown in Figure 5.25. The beamwidth match is excellent for azimuth angles within $\pm 125^\circ$. Using channels in the TE model reduced the edge currents from the finite ground plane, seen in Figure 5.23. Nulls in the back radiation region indicate edge currents still affect the pattern. Nevertheless, good agreement with the TM model is achieved within the subtended half-angle region $\pm 88^\circ$.

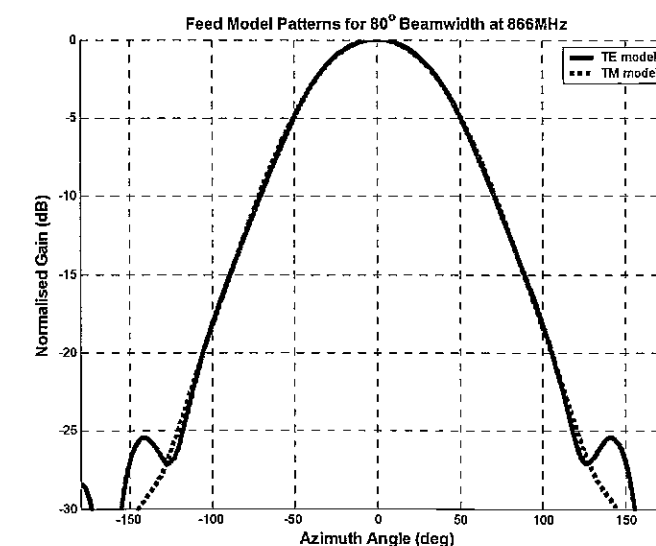


Figure 5.25 Comparison of 80° beamwidth patterns for the TE model, using channels, and TM model at 866 MHz.

Similar to the TM model in Section 5.5.1, the position of the sources can be adjusted in the TE model to produce a pattern with a range of beamwidths, with the channels minimising ground plane edge effects. The use of channels allows greater beamwidth tuning flexibility. TM and TE models are used to generate patterns which match the measured line feed patterns, in Chapter 7. These models are then included in a reflector analysis, described in Chapter 8, to determine reflector patterns for the measured feed.

5.6.4 Wideband Performance

Currently the MOST operates with a 3 MHz instantaneous bandwidth at 843 MHz and the change in reflector pattern performance across this bandwidth is negligible. The new wideband line feed will operate with a 100 MHz instantaneous bandwidth over a 1.7:1 frequency interval in the observation range 500–1000 MHz, which is likely to cause a variation in reflector pattern performance. Because the MOST is a symmetrically fed reflector, some received signals are scattered between the feed ground plane and reflector vertex, creating a standing or secondary scattered wave. As the frequency range is extended, there is a sinusoidal variation of antenna gain due to the standing wave, with a frequency, ΔF , dependent on the distance between the ground plane and reflector (Hannan 1954):

$$\Delta F = \frac{c}{2f} \quad (5.50)$$

Where c = speed of light
 f = reflector focal length

Simulated reflector pattern performance across 500–1000 MHz is presented in this section to investigate the standing wave effect. Characterisation of this variation allows corrections to be applied during calibration. In the simulations, a TM model was used to generate an 80° beamwidth feed pattern at the centre frequency, 866 MHz. Figure 5.26 shows a simulation over 500–1000 MHz, to determine the variation in beamwidth. An equivalent TE model was used to produce patterns with a similar beamwidth variation as the TM model, as described in Section 5.6.3. Once the feed patterns for the TM and TE models have been simulated across the frequency range, they are used in the combined feed/reflector model to determine the reflector pattern performance. Reflector pattern parameters are shown in Figures 5.27 to 5.29 for the gain, beamwidth and sidelobe variation across the frequency range.

Simulated half-power beamwidth variation for the TM model, in Figure 5.26, was 78°–84° across the 500–1000 MHz frequency range. Figure 5.27 shows a periodic reflector pattern gain variation with frequency for both TM and TE components. The gain increases with frequency, due to the increased electrical collecting area of the reflector at higher frequencies. The half-power beamwidth for both TM and TE reflector patterns in Figures 5.28(a) and 5.28(b), show the same periodic variation with frequency. Beamwidth peaks correspond to a gain reduction. Reflector pattern sidelobe levels across the frequency range, shown in Figure 5.29, remain < -16 dB for the TM component and are < -15 dB for the TE component.

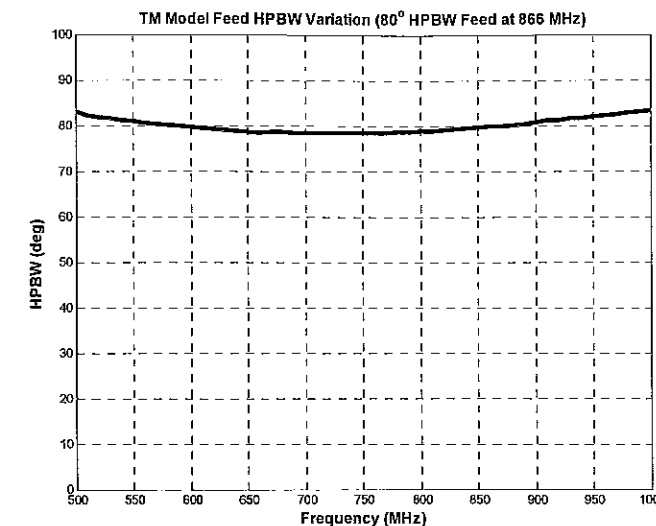


Figure 5.26 TM feed pattern HPBW for 500–1000 MHz.

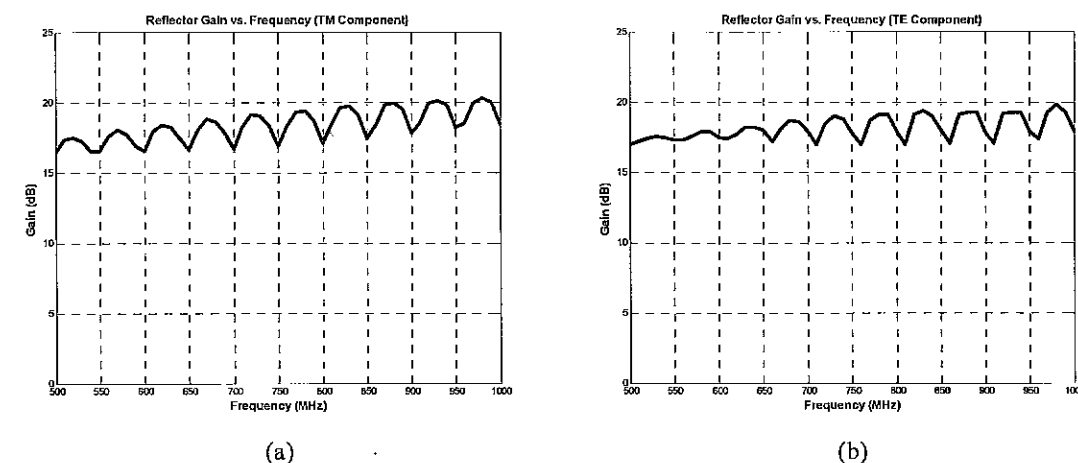


Figure 5.27 Reflector pattern gain for 500–1000 MHz. (a) TM component. (b) TE component.

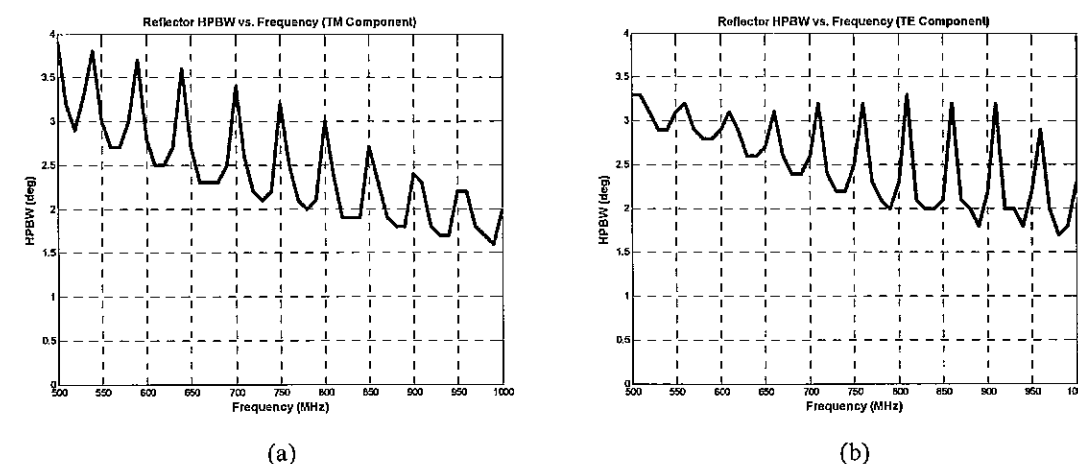


Figure 5.28 Reflector pattern HPBW for 500–1000 MHz. (a) TM component. (b) TE component.

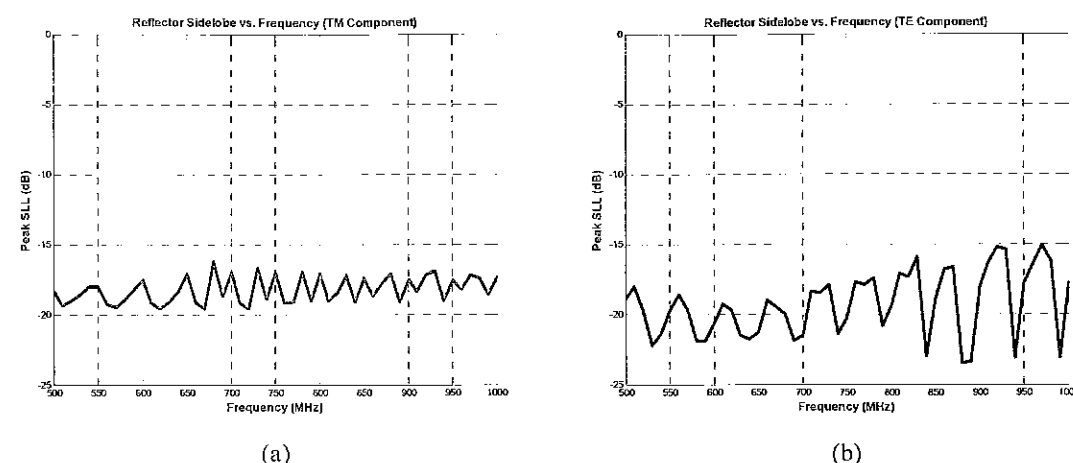


Figure 5.29 Reflector pattern sidelobes for 500–1000 MHz. (a) TM component. (b) TE component.

A distance of 3 m separates the MOST reflector vertex and ground plane. The gain variation period calculated using Equation 5.50 is 50 MHz. The equivalent simulated reflector gain and beamwidth variation period shown in Figures 5.27 and 5.28 is 50 MHz. This agreement confirms that the variation is due to the standing wave between the ground plane and reflector. Techniques to reduce the gain and beamwidth variation with frequency include using offset-fed reflector geometry and reducing the ground plane width. However, implementing these techniques at the MOST is difficult due to the existing centre-fed geometry and fixed ground plane width. An alternative solution is to place an apex plate or a spoiling structure at the reflector vertex to redirect the secondary scattering wave away from the feed (Hannan 1954; Mills 1981).

5.7 Summary

A transverse beam model was generated to characterise the reflector pattern in the N-S plane. This model was used to determine the transverse feed beamwidth range that produced the optimum sensitivity, A_{eff}/T . In addition, it enabled a focal region analysis used to evaluate the performance of the two feed configurations described in Section 4.3. An electromagnetic formulation was used in the model to solve for the scattered currents on the reflector surface, thereby including effects such as edge diffraction, reflector curvature and ground plane blockage. The rectangular aperture of the cylindrical reflector enabled the separation of the electromagnetic fields into transverse magnetic (TM) and transverse electric (TE) components, which simplified the analysis. The electromagnetic fields were solved for the cylindrical reflector using a method of moments technique.

A TM analysis was used in the feed model analysis (Section 5.5.1) because finite edge effects from the ground plane are minimised and it is therefore easier to control the shape of the pattern. For the MOST reflector geometry, an ideal feed half-power beamwidth range is 70° – 100° because it would provide spillover temperatures < 4 K and aperture efficiencies around 0.43–0.52. A reflector pattern analysis was performed, which validated the selected beamwidth range. Results showed that the major contribution to the noise temperature from the line feed radiation, was due to spillover from the feed pattern rather than the reflector curvature or blockage. A focal plane analysis described in Section 5.6.1 investigated the effects of displacing the feed along the x - and y -axes on the

reflector pattern. As the feed was displaced in the x -direction outside $\pm 0.1\lambda$ from the focal point, the reflector pattern became defocused, showing null-fill between the sidelobes. Reflector pattern results for y -directed feed displacement show that the beam centre shifts and there is a slight decrease in gain and increase in sidelobes, but they remain less than -13 dB within $\pm 0.15\lambda$ of the focal point. The rotating turret is the preferred feed configuration, because the feeds remain fixed at the reflector phase centre and are not affected by defocusing effects. Minimisation of the finite ground plane edge effects for the TE model was required in order to match its beamwidths with the TM model. This was achieved by placing a pair of channels, positioned symmetrically about the centre of the ground plane. The reflector performance over a 500–1000 MHz frequency range for both TM and TE components was carried out to investigate the sinusoidal gain variation with frequency created by the standing wave between the feed ground plane and reflector vertex. The simulations showed a periodic gain and beamwidth variation had a frequency of 50 MHz, which agreed with the calculated result.